Impact of non-equilibrium molecular packings on singlet fission in microcrystals observed using 2D white-light microscopy

Andrew C. Jones, Nicholas M. Kearns, Jia-Jung Ho, Jessica T. Flach and Martin T. Zanni*

Singlet fission, the process of splitting a singlet exciton into two triplet excitons, has been proposed as a mechanism for improving the efficiency of future photovoltaic devices. In organic semiconductors exhibiting singlet fission, the geometric relationship between molecules plays an important role by setting the intermolecular couplings that determine the system energetics. Here, we spatially image TIPS-pentacene microcrystals using ultrafast two-dimensional white-light microscopy and discover a low-energy singlet state sparsely distributed throughout the microcrystals, with higher concentrations at edges and morphological defects. The spectra of these singlet states are consistent with slip-stacked molecular geometries and increased charge-transfer couplings. The picosecond-timescale kinetics of these low-energy singlet states matches that of the correlated triplet-pair state, which we attribute to singlet/triplet-pair interconversion at these sites. Our observations support the conclusion that small populations of geometries with favourable energetics can play outsized roles in singlet fission processes.

singlet fission in small-molecule organic semiconductors has generated immense scientific interest due to its potential for increasing photovoltaic efficiencies beyond the Shockley-Queisser limit^{1,2}. In most photovoltaic materials, each absorbed photon produces a single electron with the potential for generating electricity. However, some materials, such as TIPS-pentacene (6,13-bis(triisopropylsilylethynyl)pentacene, TIPS-Pn)^{3,4}, exhibit carrier multiplication via conversion of a singlet exciton into two triplets¹. Each triplet exciton can go on to produce an electron, thereby increasing the total potential photocurrent. Indeed, pentacene-based devices have exhibited >100% internal quantum efficiencies⁵⁻⁷, indicating that more electrons are generated than photons absorbed.

The dynamics of singlet fission has been studied in a variety of sample morphologies ranging from single crystals⁸⁻¹³ to molecular aggregates^{11,14,15} and polycrystalline/disordered thin films^{13,16-19}. Here, local morphology plays a critical role as the relative geometry between molecules determines the couplings responsible for singlet fission and exciton diffusion. Intermolecular coupling has been explored via covalently tethered dimers²⁰⁻²⁴ and crystal polymophs^{25,26} where even subtle variations affect fission rates^{13,16}, efficiencies, and diffusion to sites favourable to fission²⁷.

Despite the importance of molecular packing in determining the kinetics of singlet fission, the role of intermolecular geometries and local morphology is not well understood. Non-equilibrium molecular packing is usually thought to be detrimental as it is associated with defects that recombine or trap excitons. However, defects have also been invoked to explain anomalously high triplet diffusion rates in crystals by enabling singlet and triplet interconversion^{8,9}. As a consequence, low populations of particular molecular geometries may be playing outsized roles in governing singlet fission dynamics. Identification of these geometries, however, is challenging, as sample morphologies are difficult to control on the nanoscale while the spectroscopic signature of low-population geometries is likely to be overwhelmed by more abundant signals.

We study the effects of molecular geometry on singlet fission dynamics using ultrafast two-dimensional white-light (2DWL) spectroscopy and broadband transient absorption (TA) imaging of individual TIPS-Pn microcrystals. These 2DWL spectra identify the presence of a low-population geometry whose abundance is spatially mapped via TA imaging, revealing a spatial correlation with microcrystal edges, crystal interfaces and other morphological irregularities. The observed spectral variation is modelled through the presence of a slip-stacked non-equilibrium molecular geometry whose intermolecular coupling creates singlet eigenstates at slightly reduced energy levels. These non-equilibrium geometries exist at low densities throughout the microcrystals and may play a role in singlet/triplet exchange, as evidenced by a shared picosecond timescale between low-energy singlet and localized correlated tripletpair states^{15,28-31}. From these observations and others, we conclude that the singlet energies created by the non-equilibrium molecular geometries act as a pathway for resonant energy interconversion between singlet and triplet exciton populations^{8,9}. Our observations provide insight into how non-equilibrium molecular geometries, even when present at low concentrations, can impact the kinetics of singlet fission by introducing large couplings and fortuitously placed eigenstates.

Results

The energy level diagram of the exothermic process of singlet fission in TIPS-Pn, as well as the singlet vibronic progression present in the absorption spectrum, are displayed in Fig. 1a and its inset. Previously, the kinetics of singlet fission for various forms of TIPS-Pn has been assigned to a wide range of timescales from ~0.1 ps (refs. ^{28–30,32–34}) to several picoseconds^{10–12,14}. For the microcrystals studied here, a fast decay of the singlet ground-state bleach (GSB) associated with a reduction of singlet simulated emission provides initial evidence that fission occurs on an ~100 fs timescale.

2DWL microscopic characterization. To first characterize a macroscopic ensemble of TIPS-Pn microcrystals, 2DWL spectra were

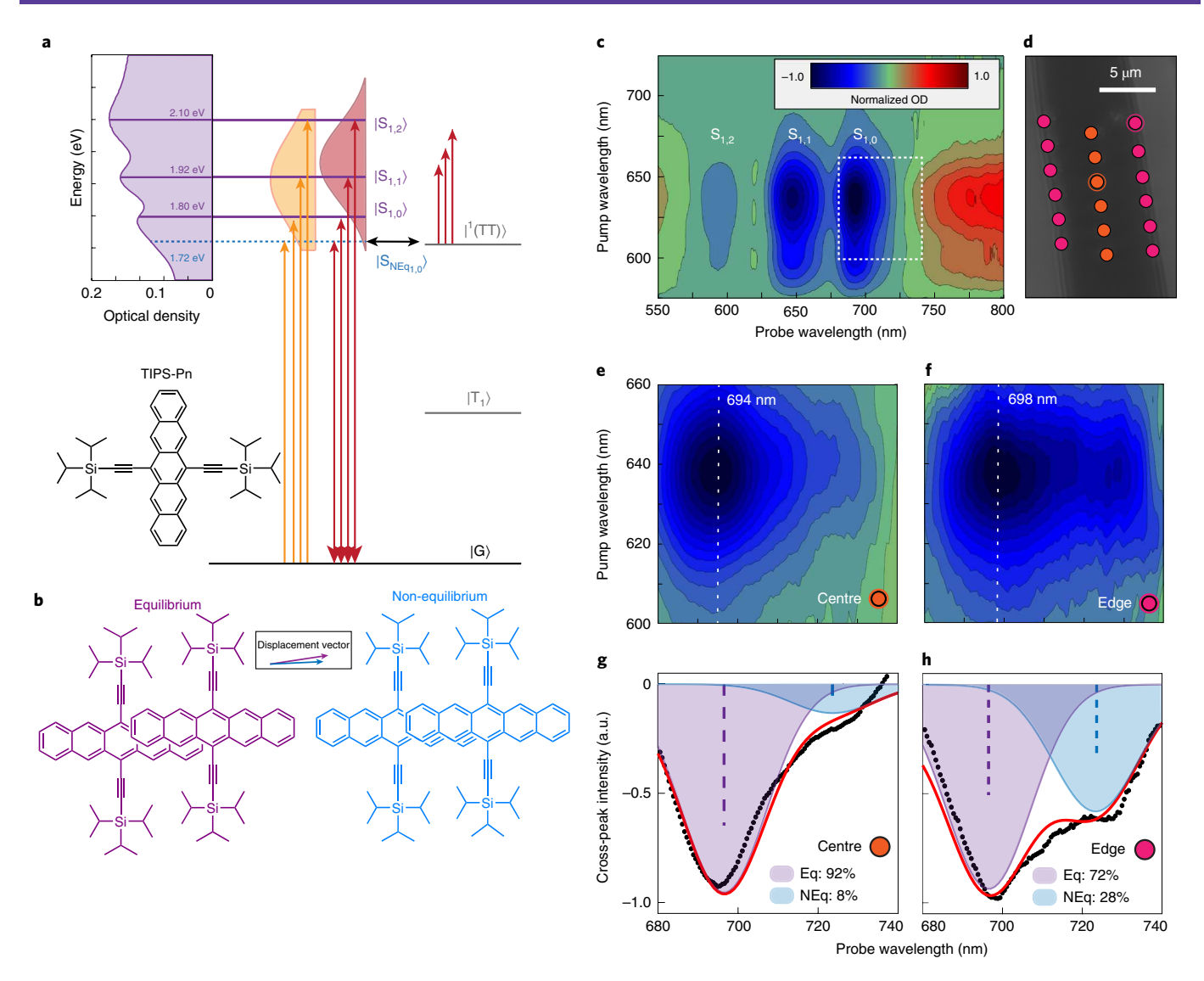


Fig. 1 | Probing energy levels using 2DWL spectroscopy. a, Singlet and triplet energies in crystalline TIPS-Pn (solid violet lines) and singlet non-equilibrium state (NEq) energies (dashed blue line). Inset: ensemble absorption spectrum of TIPS-Pn microcrystals. **b**, The relative intermolecular geometry and associated displacement vector between neighbouring molecules is pictured for equilibrium and the proposed slip-stacked non-equilibrium molecular packing configurations. **c**, 2DWL spectra corresponding to probe polarization perpendicular to the pentacene cores (delay T = 1ps). OD, optical density. **d**, Microscopy image of a single TIPS-Pn microcrystal with locations of measured 2DWL spectra. **e,f**, The $S_{1,1}$ - $S_{1,0}$ cross-peak region from single 2DWL spectra recorded at the centre (**e**) and edge (**f**) of a single TIPS-Pn microcrystal shown by matching markers in **d**. **g,h**, Horizontal cuts through the 2DWL spectra from **e** and **f**, respectively (black). Spectral fits (red) are generated using a superposition of equilibrium and non-equilibrium responses. The spectral position and strength of absorption features associated with equilibrium (dashed purple lines) and non-equilibrium (dashed blue lines) states are shown.

recorded with orthogonally polarized pump and probe pulses with a delay of T=1 ps to characterize the electronic states after singlet fission was complete (Fig. 1c). The three negative cross-peaks are associated with the GSB of the singlet vibronic progression ($S_{1,n}$) while the broad positive peak is created by weak triplet-associated excited state absorption (ESA)³⁵. For this measurement, the probe polarization is perpendicular to the longitudinal crystal axis to minimize triplet ESA and better resolve the $S_{1,n}$ progression whose transition dipole moments are oriented along the longitudinal and transverse axes of the pentacene core, respectively (Supplementary Fig. 6)^{10,11}.

The GSB cross-peak associated with the lowest energy $S_{1,0}$ absorption feature is enclosed by the dashed box in Fig. 1c. To analyse the spatial dependence of this feature, 2DWL spectra were recorded with <1 μ m spatial resolution. Representative 2DWL spectra collected at the centre (orange) and edge (pink) of a single microcrystal

are shown in Fig. 1e,f. In the centre, the $S_{1.0}$ cross-peak occurs at λ_{pump} = 638 nm and λ_{probe} = 694 nm. At the microcrystal edge, however, the probe absorption redshifts and broadens to longer wavelengths, creating a pronounced spectral shoulder illustrated by horizontal cuts through the cross-peaks shown in Fig. 1g,h. Here, at λ_{probe} = 723 nm a fourfold increase in intensity occurs in spectra near the microcrystal edge. Although the intensity and distribution of the $S_{1.0}$ cross-peak varies in magnitude and extent from crystal to crystal, the spectral shoulder is systemically larger at the microcrystal edge as compared to the centre.

Broadband TA spatial mapping. To map the spatial variation of the optical response, images were created using broadband TA microscopy. Figure 2a presents TA spectra averaged across areas at the centre (blue box in Fig. 2b) and edge (purple box in Fig. 2b) of a single

ARTICLES NATURE CHEMISTRY

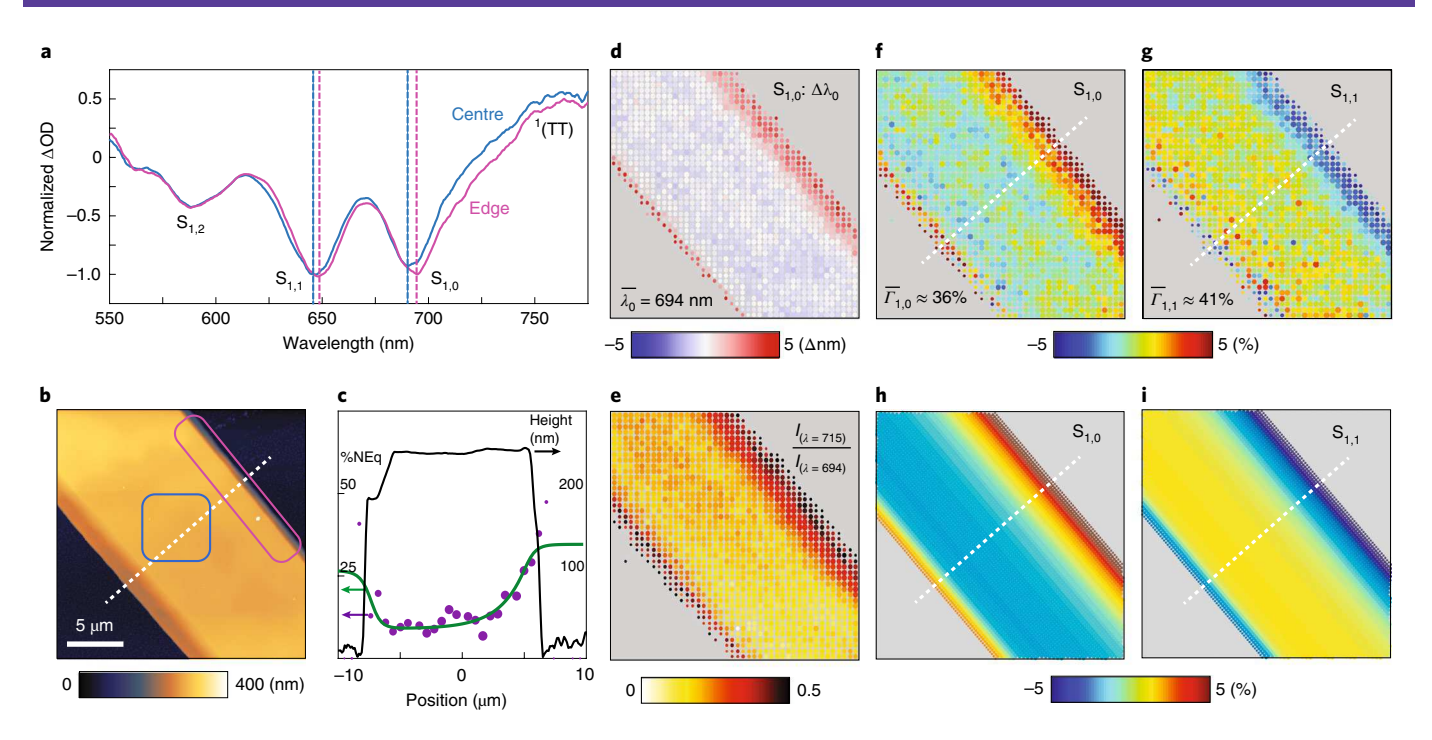


Fig. 2 | Broadband TA imaging of individual microcrystals. a,b, TA spectra (delay = 1ps) (**a**) recorded at the centre and edge regions of a single TIPS-Pn microcrystal, correlated with AFM topographic mapping (**b**). **c**, Cross-section of the AFM topography (black) with the experimentally derived (purple markers) and fitted (green) distribution of the fraction of non-equilibrium molecular packing (see Discussion). **d**, Processed TA image, displaying the relative spectral shift relative to $\overline{\lambda_0} = 694$ nm of the $S_{1,0}$ GSB, with centre and edge regions used for the TA spectra in **a** shown in blue and orange, respectively. **e**, The $S_{1,0}$ shoulder ratio, defined as the ratio of the relative intensity, *I*, of the centre of the $S_{1,0}$ GSB (694 nm) to the $S_{1,0}$ shoulder (715 nm). **f**.g, Relative variation of the fraction of singlet intensity ($\Gamma_{1,1}$) associated with the $S_{1,0}$ and $S_{1,1}$ absorption with respect to the total $S_{1,n}$ GSB progression. Mean singlet intensities are $\overline{\Gamma}_{1,0} = 36\%$ and $\overline{\Gamma}_{1,1} = 41\%$, respectively. **h**.i, Simulated intensity variation for the $S_{1,0}$ and $S_{1,1}$ GSB absorption features using the relative intensity of the GSB features in **f**.g and the modelled crystal distribution in **c**. The marker size in **c-i** indicates the strength of the TA signal.

microcrystal. The edge spectra exhibit a shifted S₁₀ bleach with a pronounced low-energy shoulder. Hyperspectral images were created by analysing the TA spectra, pixel by pixel, by fitting the S_{10} bleach to a Gaussian distribution. Identifying the average centre wavelength of the TA ($\lambda = 695 \, \text{nm}$), we created an image that identifies a systematic redshift along the lengths of both edges relative to the microcrystal centre. This redshift of up to ~5 nm (13 meV) spatially extends up to 3 µm from the edges. The edges themselves, however, are more discrete, as measured by atomic force miscroscopy (AFM) topography (Fig. 2b). Determining the ratio of the low-energy shoulder absorption at $\lambda = 715$ nm to that at the centre of the S_{10} bleach at $\lambda = 695$ nm for each TA spectrum, we created a map of the relative strength of the $S_{1,0}$ absorption shoulder (Fig. 2e). Here, the shoulder in the 2DWL spectrum is most prominent along the edges, peaking at 50% of the intensity of the S_{10} peak. Although subtle, similar redshifts in the absorption spectra have previously been observed correlated with sample preparation³⁶. The clear resolution of spectral shifts in the 2DWL spectra emphasizes the advantage of nonlinear spectroscopy techniques, which are more sensitive to changes in transition dipole strength³⁷. Moreover, the broad bandwidth of 2DWL imaging allows the entire S_{1,n} progression to be simultaneously measured, with Fig. 2f,g showing the relative intensity $(\Gamma_{1,i})$ of the $S_{1,0}$ and $S_{1,1}$ transitions, respectively. Here, the relative strength of the S_{1,0} absorption is larger near the microcrystal edge, while the $S_{1,1}$ absorption feature is correspondingly smaller. The $S_{1,2}$ state remains relatively unchanged.

To determine whether the spectral signatures associated with microcrystal edges are created by non-equilibrium molecular packing, we measured the optical response of both natural and artificially induced morphological defects. Similar redshifts and broadening of the $S_{1,0}$ transition were observed in TA mappings of crystal

interfaces (Fig. 3a), while a low-energy S_{1,0} shoulder was also resolved in 2DWL spectra (Fig. 3c). We also artificially induced structural deformations by mixing precursor molecules—6,13-pentacenequinone (PQ)—with TIPS-Pn before crystal formation³⁸⁻⁴⁰. A known impurity, PQ precipitates upon crystallization on the edges of the microcrystals (Fig. 3b, left). Adjacent to these precipitates, the S_{1.0} transition is redshifted (Fig. 3b, middle), there is an increase in the S_{1.0} sideband ratio (Fig. 3b, right) and a broad shoulder appears in the 2DWL spectrum (Fig. 3e and Supplementary Fig. 15). The results are consistent with non-equilibrium molecular packing, caused by PQ perturbing crystallization or residual PQ remaining within the microcrystal. Thus, from the combined data recorded at the edges, structural interfaces and PQ-induced deformations, we conclude that the observed intensity at wavelengths >710 nm corresponds to low-energy singlet states created by non-equilibrium molecular packing $(S_{NEq_{1,0}})$. This conclusion is further supported by wide-field fluorescence imaging, which exhibited enhanced fluorescence near edges (Fig. 3g) and spectral characterization of the fluorescence (Fig. 3h) consistent with triplet-triplet annihilation (Supplementary Section 3).

Spectral modelling. To interpret the observed TA and 2DWL spectra, we modelled the optical response of a pair of TIPS-Pn molecules as a coupled dimer using a Holstein-type Hamiltonian that includes charge-transfer states ⁴¹. The main features in the spectra were modelled using the equilibrium crystal structure. We found that the non-equilibrium features can be reproduced by a combined slip displacement from the equilibrium crystal structure of ~ 0.7 Å along the transverse and ~ 0.6 Å along the longitudinal coordinate. Shifts of this magnitude for the centre-of-mass distance between molecule pairs have been observed in TIPS-Pn polymorphs ⁴². For the slipped

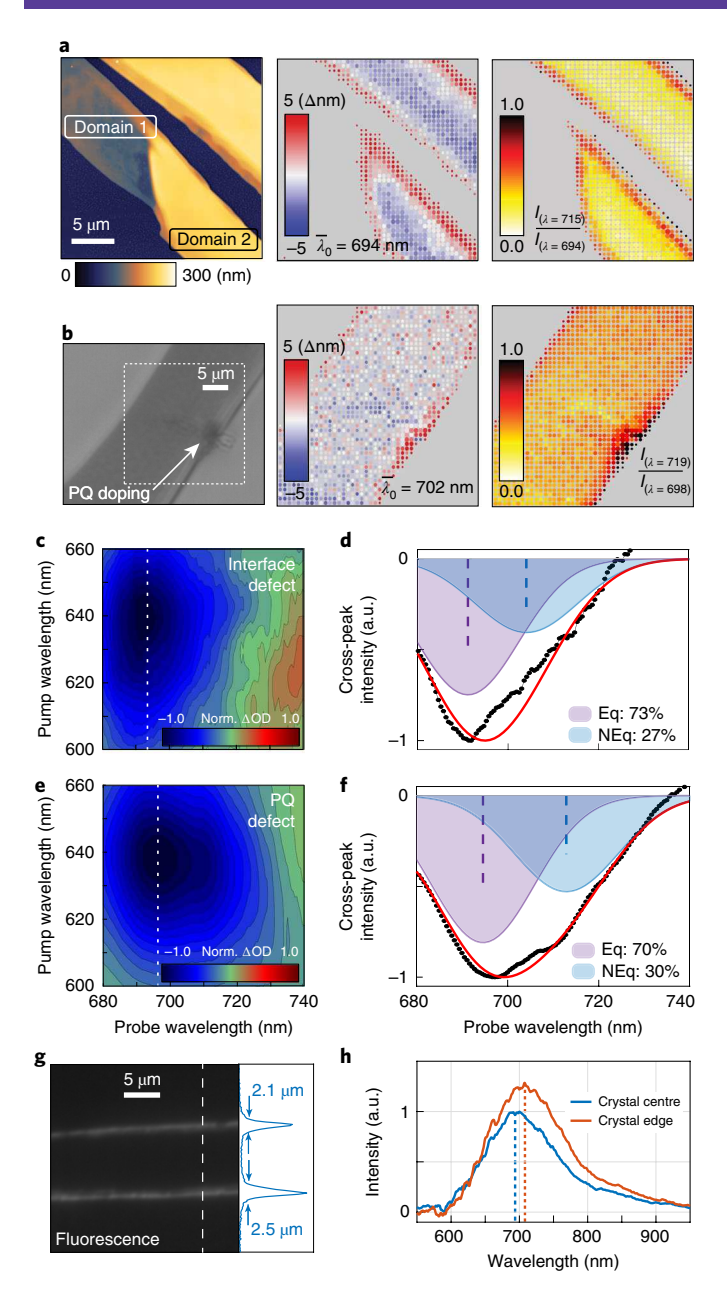


Fig. 3 | Characterization of morphological defects. a,b, TA images illustrating the variance at structural grain boundaries (a) and PQ defects (b), respectively. Left: crystallite morphology. Middle: the peak position map for the S₁₀ transition, Right: the ratio of the centre of the S₁₀ GSB to sideband. c,e, 2DWL spectra measured at interface defects (c) and defect sites in a PQ-doped TIPS-Pn microcrystal (e), demonstrating the spectral shifts and emergence of a low-energy shoulder. d,f, The corresponding horizontal spectral cuts through the cross-peak (black), with the model spectra (red) used to derive the non-equilibrium density. The spectral position and strength of the equilibrium (dashed purple) and non-equilibrium (dashed blue) singlet states are shown. g, Representative wide-field fluorescence image of a TIPS-Pn microcrystal with a line trace exhibiting enhanced fluorescence near edge regions on micrometre length scales. h, Confocal measurement of the fluence-dependent fluorescence spectrum measured from centre (blue) and edge (orange) regions of an individual microcrystal.

geometry, the hole transfer integral significantly increases in magnitude while the electronic coupling term *J* remains nearly unchanged from the equilibrium geometry, consistent with calculations⁴³.

Thus, from the combined 2DWL spectra and TA imaging across a variety of samples, we added an additional eigenstate to our energy level diagram in Fig. 1a. We placed the energy of this eigenstate at 1.72 eV and assigned it to singlets created by non-equilibrium slip-stacked molecular packing, $S_{\rm NEq_{1,0}}$. Although this energy represents the central energy, we note that the width of the cross-peaks observed in the edge- and defect-associated 2DWL spectra (Figs. 1f and 3f) reach as low as 1.65 eV. Notably, while we model only a single molecular geometry, these slip-stacked molecular packing configurations probably exist as a distribution within the microcrystal, explaining why the observed low-energy spectral shoulder is broader in samples with morphological defects (Fig. 3e,f).

Having established coupling parameters for equilibrium and non-equilibrium geometries, we find that the 2DWL spectra and the entire TA images can be fit using the relative population fraction of each geometry. In this manner, we can extract the spatial distribution of the non-equilibrium molecular packing. The 2DWL spectra measured at the centre and edge regions of a pure TIPS-Pn microcrystal (Fig. 1e,f) are reproduced by a linear combination of equilibrium to non-equilibrium packing of approximately 92:8 and 72:28, respectively, while the spectra recorded at grain boundaries and PQ defects are fit with ratios of 73:27 (Fig. 3d) and 70:30 (Fig. 3f), respectively, with a relative precision of $\pm 5\%$ (Supplementary Section 7).

Utilizing data from the broadband TA maps, the spatial distribution of non-equilibrium molecular packing can be determined as shown by the data cross-section of an individual microcrystal (Fig. 2c). Using a fit of non-equilibrium molecular packing and convolving with the spatial resolution of the microscope, simulated TA maps of the spatial variation of the S_{1,0} and S_{1,1} absorption features are generated (Fig. 2h,i) that reproduce those observed experimentally (Fig. 2f,g). From the fits, we find that the density of the non-equilibrium molecular geometry occurs at lower densities (~3–10%) in centre regions and higher densities (up to 40%) at the microcrystal edges.

Kinetics characterization. To assess the effect of $S_{\mathrm{NEq}_{1,0}}$ states upon fission, TA kinetics were collected for both oriented ensembles of microcrystals (Fig. 4a-c) and targeted locations within single microcrystals (Fig. 4e). In ensemble measurements, we characterized the dynamics of the singlet population by orienting the pump and probe polarizations along the short axis of the pentacene cores within the microcrystal to selectively excite and probe the S_{1,n} progression. As shown in Fig. 4c,d, we observe both ~100 fs and picosecond time constants in the response. Following photoexcitation of the $S_{1,n}$ states, the singlet GSB decreases in magnitude over the following 100 fs, indicating a reduction in stimulated emission. Mirroring these kinetics, triplet ESA increases (Fig. 4c) while a transient ESA feature at ~620 nm (Fig. 4d, blue line), attributed to absorption by singlets to higher singlet excited states $(S_1 \rightarrow S_m)$ similar to that of crystalline pentacene⁴⁴, has a 100 fs timescale. Taken together, this mutual timescale indicates that singlet fission occurs with a $\tau_{\rm sf} \approx 100 \, \rm fs$ time constant, in agreement with several recent measurements^{28-30,32-34} and in contrast to others assigning rates to picosecond timescales10-12,14.

Figure 4a displays an ensemble TA response measured with orthogonal pump/probe orientations with the probe oriented along the longitudinal axis of the molecular cores of the microcrystal. This polarization combination selectively excites a singlet population but probes the ESA associated with triplet states. In this case we measure the same $\sim 100 \, \mathrm{fs}$ rise in broadband triplet ESA that was assigned to singlet fission above, followed by a decay ranging from 625 to 750 nm that occurs over several picoseconds. The picosecond timescale is illustrated in Fig. 4b, which presents the spectral distribution of the response after subtraction of the offset at $T=25 \, \mathrm{ps}$, revealing an ESA feature with a centre energy of 1.77 eV and bandwidth of 0.1 eV that decays on a $\sim 3 \, \mathrm{ps}$ timescale. This energy range is

ARTICLES NATURE CHEMISTRY

consistent with recent observations of ESA from a localized correlated triplet-pair state (${}^{1}(TT)$, ${}^{1}(TT) \rightarrow S_{m}$) in pentacene dimers 31,45 , while the timescale matches previous measurements ${}^{15,28-30}$ of the ${}^{1}(TT)$ state prior to separation to a dissociated but still spin-coherent correlated triplet-pair state ${}^{1}(T...T)^{31,46}$. We correspondingly assign this broadband near-infrared ESA feature to the presence of ${}^{1}(TT)$ exciton pairs, which thus allows us to track the kinetics of its population.

Recognizing that the ~3 ps timescale for 1(TT) ESA is similar to that observed for $S_{1,0}$ and $S_{NEq_{1,0}}$ GSB (Fig. 4d), we performed a global fit of the data to determine the system kinetics (Supplementary Section 9). A combined feature representing the lowest energy vibronic absorption for equilibrium and non-equilibrium molecular geometries ($S_{1,0}$ and $S_{NEq_{1,0}}$) is displayed because the population of the non-equilibrium geometries is small on average. Fits of the TA spectra and their kinetics are shown in Fig. 4b-d (black dashed lines). As the broad near-infrared spectral distribution of the triplet ESA differs from specific wavelengths associated with the vibronic progression of the singlet GSB, these fits of the picosecond-timescale triplet and singlet population kinetics do not interfere with one another. From these fits, we obtain timescales for the 1(TT) ESA and low-energy singlet GSB with constants of 3.2 ± 0.3 ps and 2.9 ± 0.6 ps, respectively. The equality of these time constants suggests that these populations are connected by a shared physical mechanism.

To further understand the impact of non-equilibrium molecular packing on singlet fission, we performed analogous kinetics measurements at microcrystal edge regions (similar to the positions displayed in Fig. 1d), where the proposed slip-stacked packing reaches up to 40%. The extracted TA data in Fig. 4e display the kinetics of the $S_{1,0}$ and $S_{NEq_{1,0}}$ GSB features as well as the $^1(TT)$ ESA (measured at 695, 725 and 755 nm, respectively). The dynamics of these states appear qualitatively similar to those measured for the microcrystal ensemble with the exception that the approximately picosecond deepening of the GSB occurs specifically in association with the non-equilibrium singlet state, $S_{NEq_{1.0}}$. In previous studies, others¹¹ observed picosecond timescale dynamics at both edge and centre regions of individual microcrystals, with edge and interfacial regions exhibiting slightly faster dynamics. Additionally, small structural variations between crystal polymorphs have been observed to affect the picosecond timescale dynamics in thin films²⁹. In our broadband measurements, we observe similar picosecond dynamics at both the bulk and edge regions of the microcrystals. Notably, the relative change in the magnitude associated with approximately picosecondtimescale dynamics (100 fs to 10 ps) is \sim 30% for both the $^{1}(TT)$ ESA and the $S_{NEq_{1.0}}$ GSB. Here, the ESA associated with the $^{1}(TT)$ state decreases in magnitude while the GSB of the $S_{NEq_{1,0}}$ state continues to deepen (Fig. 4e). Corresponding kinetic fits find that the $S_{NEq_{1,0}}$ GSB grows with a time constant of 2.1 ± 0.4 ps while the ¹(TT) ESA similarly decreases with a constant of 2.5 ± 0.5 ps. Thus, the kinetics of low-energy singlet states associated with non-equilibrium molecular geometries and the ¹(TT) state match within error.

Discussion

As evidenced by the broadband 2DWL and TA microscopy measurements, a fraction of TIPS-Pn molecules exhibit a spectral response consistent with non-equilibrium packing. We model this using a sub-ångstrom slip-stacked lattice distortion. This distortion alters the π -stacking between neighbouring molecules to create much larger charge-transfer coupling, resulting in a reduction of the singlet state energy. The observed spectra cannot be reproduced by Stark effects⁴⁷, ionic doping^{48,49}, temperature-dependent absorption⁵⁰ or other factors that induce local electrostatic effects (Supplementary Section 2). Spatial TA imaging reveals that while non-equilibrium packing is present throughout microcrystals at low densities (3–10%), it can be found at higher densities (up to 50%), which are spatially correlated with microcrystal edges and other

morphological defects where the crystallization process occurs under non-uniform conditions. The observed spatial variation and the nonlinear scaling of the 2DWL signal aided in the recognition of the presence of these non-equilibrium spectral features, which are much less pronounced in ensemble and linear spectra.

Using the above data (Fig. 4a-e), we propose the model depicted in Fig. 4g. Upon photoexcitation at T = 0, the $S_{1,n}$ manifold of singlet states is populated (frame (i)) and quickly interconverts to localized ${}^{1}(TT)$ states 34,46 via singlet fission with a rate, k_{SF}^{-1} (frame (ii)). Subsequently, 1(TT) excitations disperse across neighbouring molecules to form the separated but spin-correlated triplet state ¹(T...T) with the rate k_{Sep}^{-1} (frame (iii)). The distinction between localized and separated correlated triplet-pair states has been reported previously^{34,46} and is consistent with our observed picosecond-timescale decrease in ESA attributed to the ¹(TT) state. To determine the rate constants associated with these processes, we utilized the global fits of the TA data (Fig. 4a-d) to assign the time dependence of the spectral signatures of singlet fission and triplet-pair separation as $k_{\rm SF}^{-1}=95$ fs and $k_{\rm Sep}^{-1}=3.2$ ps, respectively. Similar to previous population models^{10,12,30}, we utilized these rate constants to develop an energy-transfer model that simulates singlet and triplet populations to reproduce the dynamics of their spectral signatures (Fig. 4f and Supplementary Section 9).

Although the experimentally determined $k_{\rm SF}^{-1}$ and $k_{\rm Sep}^{-1}$ rate constants explain many aspects of the data, they do not account for the observed ~3 ps timescale increase in magnitude of the $S_{1,0}$ and $S_{\rm NEq_{1,0}}$ GSB (Fig. 4c,d), nor the fact that this timescale is shared by the decrease of the ¹(TT) ESA. After excitation, a GSB feature may deepen for a number of reasons, including (1) depletion of the ground state, (2) alteration of the ground state absorption and (3) increased stimulated emission from an excited state. All but the last reason are ruled about because processes that induce local electrostatics are not consistent with the data (see above) and because depletion of the ground state due to excitation and singlet fission occur on <100 fs timescales. Thus, we assign the approximate picosecond-timescale increase in magnitude of the $S_{1,0}$ and $S_{\rm NEq_{1,0}}$ GSB to stimulated emission.

To enable this simulated emission, the singlet population must increase. We propose that localized $^{\rm l}({\rm TT})$ excitons undergo triplet fusion, that is, population transfer occurs between $^{\rm l}({\rm TT})$ and lowenergy singlet states (Fig. 4g,h). Such triplet recombination explains the increase of $\rm S_{NEq_{1.0}}$ GSB and decrease of $^{\rm l}({\rm TT})$ ESA on a shared $\sim\!\!3$ ps time constant. This energy transfer pathway is added to the population model for an individual microcrystal as a whole (in Fig. 4f) by including a fusion rate constant of $k_{\rm NEqF}^{-1}$, which is established by the branching ratio of energy transfer from $^{\rm l}({\rm TT})$ to $\rm S_{NEq_{1.0}}$ and $^{\rm l}({\rm T...T})$ states. Here, a rate of $k_{\rm NEqF}^{-1}\approx30$ ps is determined using the magnitude of the experimentally observed growth of the $\rm S_{NEq_{1.0}}$ GSB. Although triplet conversion dominates, the ensemble measurements and associated population modelling indicate that $\sim\!\!10\%$ of the localized $^{\rm l}({\rm TT})$ population experiences exchange with nonequilibrium singlet states for our microcrystals as a whole.

It is noteworthy that the ~2–3 ps timescale transfer dynamics associated with $^1(\mathrm{TT})$ separation is not shared by the full $S_{1,n}$ progression, but only the $S_{\mathrm{NEq_{1,0}}}$ and $S_{1,0}$ states. This observation is consistent with our model, but not with the alternative explanation that picosecond-timescale deepening of singlet GSB is associated with the separation of $^1(\mathrm{TT})$ exciton pairs to $^1(\mathrm{T...T})$ states, as such triplet separation would be expected to uniformly deepen the GSB of the full $S_{1,n}$ progression. The specific association of the ~2–3 ps time constant with low-energy singlet states (Fig. 4e,d) is more consistent with population exchange as the primary mechanism of the picosecond kinetics.

For fusion of localized triplet-pair states back to low-energy singlet states to occur, the energies of the low-energy singlet and $^{1}(TT)$ states would need to overlap or be within $k_{\rm B}T$. Recent measurements

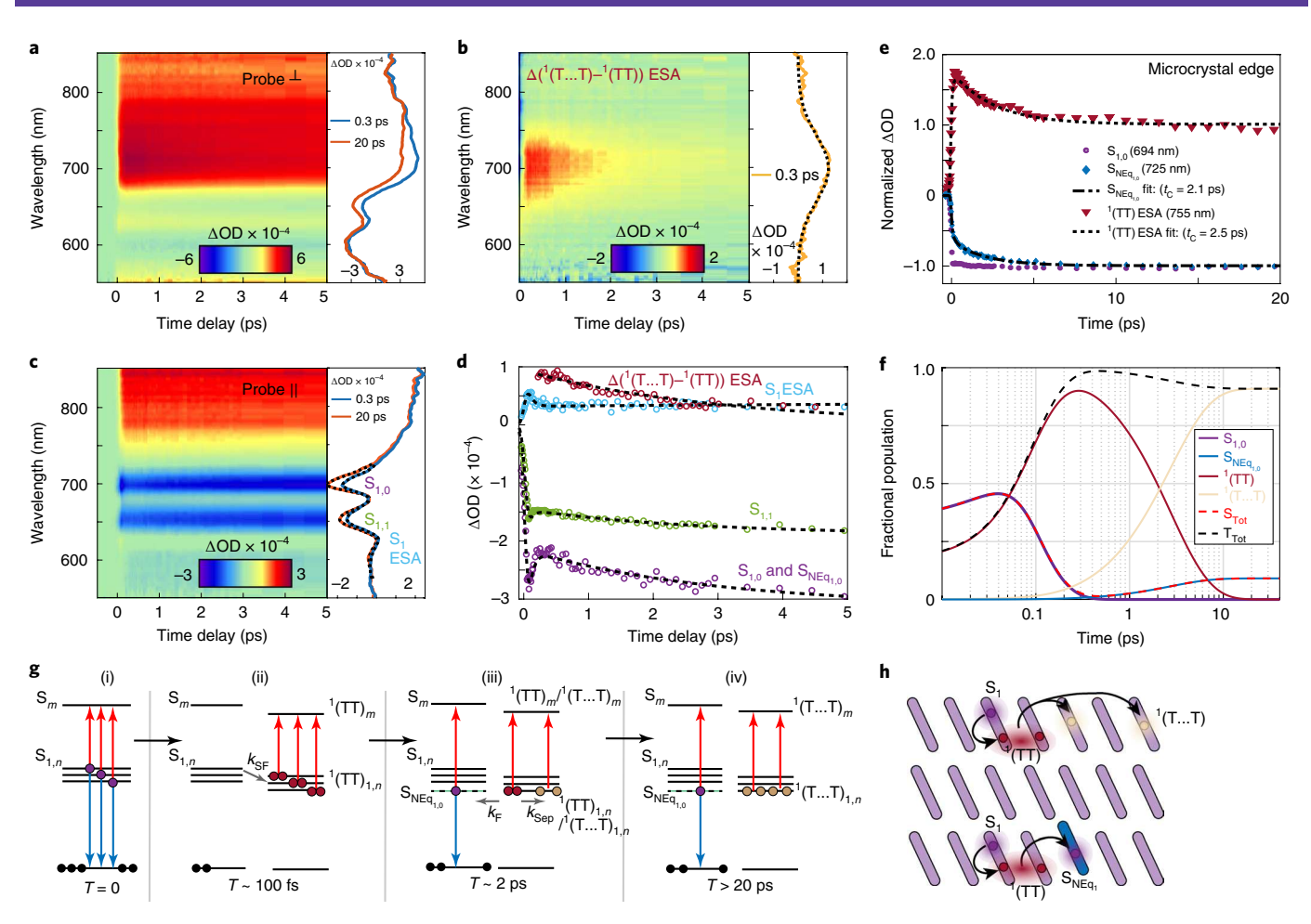


Fig. 4 | Kinetic characterization via broadband TA. a,c, TA measurements with a macroscopic (-30 μ m) focal volume with perpendicular (**a**) and parallel (**c**) relative pump/probe polarizations used to probe the '(TT) ESA and $S_{1,n}$ GSB, respectively. **b**, The picosecond timescale component of triplet ESA, attributed to the difference between '(T...T) and '(TT), which redisplays the data from **a** after subtraction of the spectral distribution of the long-timescale (T=25 ps) component of the signal. **d**, The time dependence of '(TT) ESA and the $S_{1,n}$ GSB. **e**, Corresponding TA kinetics measured from a single microcrystal edge fitted to exponentials with time-constant, t_C . **f**, The modelled singlet (red dashed) and triplet (black dashed) populations relative to the individual populations of individual $S_{1,0}$ (purple), $S_{NEq_{1,0}}$ (blue), '(TT) (maroon) and '(T...T) (beige) species based on the TA dynamics in **a-d. g**, Energy level diagrams depicting the population flow from the singlet (purple) $S_{1,n}$ manifold. **h**, Schematic of the slip-stacked molecular packing geometry that enables the observed $S_{NEq_{1,0}}$ states observed via 2DWL spectroscopy with the proposed energy pathways from measurements of TA kinetics.

of the spectral distribution of delayed emission from TIPS-Pn have been attributed to triplet-triplet upconversion/annihilation and evidence that the $S_{1,0}$ singlet energy is proximate to twice the energy of the isolated triplet state⁵¹. Our observations of 2DWL cross-peaks at 720 nm place the energy of the $S_{NEq_{1,0}}$ state at ~1.72 eV, ~70 meV lower than the $S_{1,0}$ absorption associated with the equilibrium packing. Because phosphorescence from solid-phase TIPS-Pn is weak, the triplet energy of pentacene (0.86 eV) is often cited for modelling purposes⁵². This approximation places ¹(TT) states directly on resonance with the $S_{NEq_{1,0}}$ states present in the 2DWL spectra. The states may not be exactly on resonance, however, as phosphorescence measured from TIPS-Pn monomers and dimers solvated in cryogenic methyl-tetrahydrofuran places the central 1(TT) energy at 1.58 eV. Considering the spectral distribution of triplet phosphorescence we find ~10% of the expected 1(TT) energies overlap with the $S_{1,0}$ and $S_{\mathrm{NEq}_{1,0}}$ states (Supplementary Section 5). Although this overlap would presumably be larger at room temperature, we regardless find that singlet/triplet exchange is possible for at least a fraction of molecules in non-equilibrium packing configurations.

Intermolecular couplings such as charge transfer are thought to play an important role in the process of singlet fission⁴¹. For example,

non-equilibrium packing within organic semiconductors has been proposed to create 'hot' spots that favour a specific energy transfer pathway^{16,18,27}. In acene films, it is thought that singlets diffuse to molecular geometries where couplings are favourable for singlet fission^{13,18} while slip-stacked geometries have been investigated as potential fission sites^{15,19} and invoked to explain triplet-pair intermediates in solution^{4,53}. Indeed, certain intermolecular geometries may favour population exchange between triplets and singlets, thus improving exciton diffusion^{8,9}.

Identifying the non-equilibrium molecular packing geometries and the magnitude of the charge-transfer couplings responsible for the above studies is difficult. The TIPS-Pn absorption and kinetics presented here provide a link between structure, charge-transfer couplings and the kinetics of singlet fission. According to our model, through small shifts in the intermolecular geometry, the associated increase in the charge-transfer couplings results in a clear shift in the absorption frequency. Charge-transfer couplings are thought to mediate singlet fission to a localized triplet-pair state. For the case of TIPS-Pn, these couplings also create energy overlap between low-energy singlets and the localized triplet-pair state, allowing for the possibility of population exchange between the singlet and

ARTICLES NATURE CHEMISTRY

triplet populations. We do not know if singlet/triplet exchange fosters diffusion, which would occur at a much longer timescale than measured here, but portions of these two states lie within $k_{\rm B}T$. An interesting experiment would be to correlate the population of non-equilibrium molecular packing with exciton diffusion.

Methods

Sample preparation. The TIPS-Pn microcrystals studied here were fabricated via drop-cast crystallization on a SiO_2 substrate, creating crystals $100-300\,\mathrm{nm}$ in height, $10-15\,\mu\mathrm{m}$ wide and millimetres in length (see Supplementary Section 1 for further details).

Ultrafast 2DWL microscopy system. To achieve high spatial resolution, a high repetition-rate 2DWL spectroscopy systems was coupled with a reflective optical microscope objective (NA = 0.65) to achieve <1 μm focal volumes. The focal position of collinear pump/probe beams was matched with the tip of an AFM to provide correlated subdiffraction topographic information on the sample morphology. The fluence of the broadband pump pulse (~250 μJ cm $^{-2}$) was maintained in an annihilation-free regime $^{10-12}$ corresponding to excitation densities of ~3% to avoid multiexciton effects and triplet—triplet annihilation effects (Supplementary Section 2).

TA images were generated by pixel-to-pixel scanning of the sample through the objective focus. Post-processing at each pixel was performed to determine the spectral positions and bandwidths of the $S_{1,n}$ vibronic progression, the $S_{1,0}$ sideband ratio and the fraction of singlet intensity ($\Gamma_{1,0}$). In comparison to conventional absorption spectroscopy, TA is more sensitive to small variations of the optical response, as scattering can effectively be removed (Supplementary Fig. 3). No indication of waveguiding effects via periodic variation of the TA indicating enhanced/reduced emission was observed. The spectral trends were observed across many crystals of varying thickness and relative orientation, ruling out artefacts associated with diffraction, triplet ESA interference and optical density (Supplementary Section 8). Rather, the observed spatial variation expresses real differences in the local electronic structure of the microcrystal centre versus the edge.

For Fig. 3f,g the sideband ratio was determined by taking the ratio integrated intensity of the low-energy singlet transition (715 nm) to the $S_{1.0}$ peak located at 695 nm. The fraction of singlet intensity ($\Gamma_{1,l}$) was found by taking the ratio of the integrated intensity of the singlet absorption to the integrated intensity of the GSB associated with the full vibronic progression.

Spectral modelling. Although simulations have predicted wavefunctions in TIPS-Pn to extend over several molecules 12,55 , to limit the number of model parameters we employ a simple coupled-dimer model $^{43,56-59}$ and are able to reproduce the observed presence of low-energy singlet states.

The full Hamiltonian, including vibronic states, is provided in Supplementary Section 7. For illustration purposes, we show a simplified block diagram:

$$H = \begin{pmatrix} H_{S_1S_0}^{\text{mono}} + D & J & t_e & t_h \\ J & H_{S_0S_1}^{\text{mono}} + D & t_h & t_e \\ t_e & t_h & H_{CA}^{\text{CT}} & 0 \\ t_h & t_e & 0 & H_{AC}^{\text{CT}} \end{pmatrix}$$
(1)

 H^{mono} represents the collection of terms that relate the energy of singlet excitations of non-coupled TIPS-Pn molecules to parameters representing the Frenkel excitonic energy ($\omega_0 = 15,580 \text{ cm}^{-1}$), vibrational-quanta energy ($\nu_0 = 1,310 \text{ cm}^{-1}$) and the vibronic coupling/Huang–Rhys factor ($\lambda^2 = 0.4$), arrived at from fits of the absorption spectrum of TIPS-Pn monomers in toluene solution. Chargetransfer states and couplings are incorporated via the charge-transfer Hamiltonian for cationic (C) and anionic (A) sites (HCT) and the electron and hole transferintegral coupling terms (t_e, t_h) , respectively. Recent calculations were used for the energy of these states ($\omega_{\rm CT} = 2\hat{1}$,470 cm $^{-1}$) and the transfer-integral coupling terms, which are $t_e = -1,346 \text{ cm}^{-1}$ and $t_h = -153 \text{ cm}^{-1}$ for the equilibrium packing geometry of crystalline TIPS-Pn⁴³. The relative orientations and displacements of the transition dipoles are derived from polarization anisotropy^{10,11} and the crystal structure, respectively^{38,43}. Having established these fixed parameters, only the solvatochromatic shift (D) and Coulombic coupling (J) remain as adjustable parameters. The broadband TA spectrum for the equilibrium molecular packing geometry was fit through iterative variation, yielding values of $J = 560 \,\mathrm{cm}^{-1}$ and $D = -1,165 \,\mathrm{cm}^{-1}$ to reproduce the centre frequencies and relative magnitudes of the GSB features of the S₁, vibronic progression associated with equilibrium molecular packing geometries (Fig. 1b).

We then turned to reproducing the spectral features in the data associated with non-equilibrium molecular packing. Notably, when using the charge-transfer coupling parameters (t_e , t_h) associated with equilibrium molecular geometry, there was no combination of electronic coupling/solvatochromatic shift that could simultaneously reproduce both the observed vibronic progression and the transitions at wavelengths $\lambda > 710$ nm. For π -stacked molecules such as TIPS-Pn, small changes in the slip-stacking between neighbouring molecules can result in

large variations of the charge-transfer couplings 29,59 . Accordingly, we iteratively searched potential slip-stacking geometries to fit the observed $S_{1,0}$ low-energy shoulder intensity, the $\sim\!5$ nm redshift in the $S_{1,0}$ transition (Fig. 2d), the change in relative ratios of the $S_{1,0}$ and $S_{1,1}$ transitions (Fig. 2f,g), and the absence of asymmetric sideband peaks in the $S_{1,1}$ transition. Searching the potential charge-transfer couplings associated with small shifts from equilibrium molecular packing, we found the small slip-stacked distortion noted in the main text resulted in an increase in magnitude of the hole transfer integral ($t_{\rm h} \simeq -1,500~{\rm cm}^{-1}$) while the electronic coupling term J is nearly unchanged from the equilibrium geometry (Supplementary Section $7J^{43}$. These parameters were able to successfully reproduce the presence of the low-energy singlet state.

Data availability

The experimental data with corresponding spectral simulations are available from the authors upon request.

Code availability

The MATLAB codes used for data analysis and simulations are available from the authors upon request.

Online content

Any methods, additional references, Nature Research reporting summaries, source data, extended data, supplementary information, acknowledgements, peer review information; details of author contributions and competing interests; and statements of data and code availability are available at https://doi.org/10.1038/s41557-019-0368-9.

Received: 3 January 2018; Accepted: 8 October 2019; Published online: 2 December 2019

References

- 1. Smith, M. B. & Michl, J. Singlet fission. Chem. Rev. 110, 6891-6936 (2010).
- Shockley, W. & Queisser, H. J. Detailed balance limit of efficiency of p-n junction solar cells. J. Appl. Phys. 32, 510–519 (1961).
- Ramanan, C., Smeigh, A. L., Anthony, J. E., Marks, T. J. & Wasielewski, M. R. Competition between singlet fission and charge separation in solution-processed blend films of 6,13-bis(triisopropylsilylethynyl)pentacene with sterically-encumbered perylene-3,4:9,10-bis(dicarboximide)s. *J. Am. Chem. Soc.* 134, 386–397 (2012).
- Walker, B. J., Musser, A. J., Beljonne, D. & Friend, R. H. Singlet exciton fission in solution. *Nat. Chem.* 5, 1019–1024 (2013).
- Congreve, D. N. et al. External quantum efficiency above 100% in a singlet-exciton-fission-based organic photovoltaic cell. Science 340, 334–337 (2013).
- Yang, L. et al. Solution-processable singlet fission photovoltaic devices. Nano Lett. 15, 354–358 (2015).
- Pazos-Outon, L. M. et al. A silicon-singlet fission tandem solar cell exceeding 100% external quantum efficiency with high spectral stability. ACS Energy Lett. 2, 476–480 (2017).
- Zhu, T., Wan, Y., Guo, Z., Johnson, J. & Huang, L. Two birds with one stone: tailoring singlet fission for both triplet yield and exciton diffusion length. *Adv. Mater.* 28, 7539–7547 (2016).
- Wan, Y. et al. Cooperative singlet and triplet exciton transport in tetracene crystals visualized by ultrafast microscopy. Nat. Chem. 7, 785–792 (2015).
- Wong, C. Y. et al. Revealing exciton dynamics in a small-molecule organic semiconducting film with subdomain transient absorption microscopy. J. Phys. Chem. C 117, 22111–22122 (2013).
- Wong, C. Y., Cotts, B. L., Wu, H. & Ginsberg, N. S. Exciton dynamics reveal aggregates with intermolecular order at hidden interfaces in solution-cast organic semiconducting films. *Nat. Commun.* 6, 5946 (2015).
- Folie, B. D., Haber, J. B., Refaely-Abramson, S., Neaton, J. B. & Ginsberg, N. S. Long-lived correlated triplet pairs in a π-stacked crystalline pentacene derivative. J. Am. Chem. Soc. 140, 2326–2335 (2018).
- Piland, G. B. & Bardeen, C. J. How morphology affects singlet fission in crystalline tetracene. J. Phys. Chem. Lett. 6, 1841–1846 (2015).
- Tayebjee, M. J. Y. et al. Morphological evolution and singlet fission in aqueous suspensions of TIPS-pentacene nanoparticles. J. Phys. Chem. C 120, 157–165 (2016).
- Pensack, R. D. et al. Exciton delocalization drives rapid singlet fission in nanoparticles of acene derivatives. J. Am. Chem. Soc. 137, 6790–6803 (2015).
- 16. Roberts, S. T. et al. Efficient singlet fission found in a disordered acene film. J. Am. Chem. Soc. 134, 6388–6400 (2012).
- Schnedermann, C. et al. Sub-10 fs time-resolved vibronic optical microscopy. J. Phys. Chem. Lett. 7, 4854–4859 (2016).
- Broch, K. et al. Robust singlet fission in pentacene thin films with tuned charge transfer interactions. Nat. Commun. 9, 954 (2018).

- Eaton, S. W. et al. Singlet exciton fission in polycrystalline thin films of a slip-stacked perylenediimide. J. Am. Chem. Soc. 135, 14701–14712 (2013).
- 20. Sanders, S. N. et al. Quantitative intramolecular singlet fission in bipentacenes. *J. Am. Chem. Soc.* **137**, 8965–8972 (2015).
- 21. Zirzlmeier, J. et al. Singlet fission in pentacene dimers. *Proc. Natl Acad. Sci. USA* 112, 5325–5330 (2015).
- Kumarasamy, E. et al. Tuning singlet fission in π-bridge-π chromophores. *J. Am. Chem. Soc.* 139, 12488–12494 (2017).
- Nagarajan, K., Mallia, A. R., Reddy, V. S. & Hariharan, M. Access to triplet excited state in core-twisted perylenediimide. *J. Phys. Chem. C* 120, 8443–8450 (2016).
- 24. Korovina, N. V. et al. Singlet fission in a covalently linked cofacial alkynyltetracene dimer. *J. Am. Chem. Soc.* **138**, 617–627 (2016).
- Bhattacharyya, K. & Datta, A. Polymorphism controlled singlet fission in TIPS-anthracene: role of stacking orientation. *J. Phys. Chem C* 121, 1412–1420 (2017).
- Arias, D. H., Ryerson, J. L., Cook, J. D., Damrauer, N. H. & Johnson, J. C. Polymorphism influences singlet fission rates in tetracene thin films. *Chem. Sci.* 7, 1185–1191 (2016).
- Mou, W. W., Hattori, S., Rajak, P., Shimojo, F. & Nakano, A. Nanoscopic mechanisms of singlet fission in amorphous molecular solid. *Appl. Phys. Lett.* 102, 173301 (2013).
- Grieco, C. et al. Harnessing molecular vibrations to probe triplet dynamics during singlet fission. J. Phys. Chem. Lett. 8, 5700–5706 (2017).
- Grieco, C. et al. Triplet transfer mediates triplet pair separation during singlet fission in 6,13-bis(triisopropylsilylethynyl)-pentacene. Adv. Funct. Mater. 27, 1703929 (2017).
- Grieco, C. et al. Direct observation of correlated triplet pair dynamics during singlet fission using ultrafast mid-IR spectroscopy. J. Phys. Chem. C 122, 2012–2022 (2018).
- Miyata, K., Conrad-Burton, F. S., Geyer, F. L. & Zhu, X. Y. Triplet pair states in singlet fission. Chem. Rev. 119, 4261–4292 (2019).
- Bakulin, A. A. et al. Real-time observation of multiexcitonic states in ultrafast singlet fission using coherent 2D electronic spectroscopy. *Nat. Chem.* 8, 16–23 (2016).
- Herz, J. et al. Unveiling singlet fission mediating states in TIPS-pentacene and its aza derivatives. J. Phys. Chem. A 119, 6602–6610 (2015).
- Pensack, R. D. et al. Solution-processable, crystalline material for quantitative singlet fission. *Mater. Horizons* 4, 915–923 (2017).
- Yong, C. K. et al. The entangled triplet pair state in acene and heteroacene materials. Nat. Commun. 8, 15953 (2017).
- Grieco, C. et al. Dynamic exchange during triplet transport in nanocrystalline TIPS-pentacene films. J. Am. Chem. Soc. 138, 16069–16080 (2016).
- 37. Grechko, M. & Zanni, M. T. Quantification of transition dipole strengths using 1D and 2D spectroscopy for the identification of molecular structures via exciton delocalization: application to α -helices. *J. Chem. Phys.* **137**, 184202 (2012).
- Anthony, J. E., Brooks, J. S., Eaton, D. L. & Parkin, S. R. Functionalized pentacene: improved electronic properties from control of solid-state order. J. Am. Chem. Soc. 123, 9482–9483 (2001).
- Gomar-Nadal, E., Conrad, B. R., Cullen, W. G. & Willams, E. A. Effect of impurities on pentacene thin film growth for field-effect transistors. *J. Phys. Chem. C* 112, 5646–5650 (2008).
- Conrad, B. R. et al. Effect of impurities on pentacene island nucleation. Phys. Rev. B 77, 205328 (2008).
- 41. Monahan, N. & Zhu, X. Y. Charge transfer-mediated singlet fission. Annu. Rev. Phys. Chem. 66, 601–618 (2015).
- 42. Diao, Y. et al. Understanding polymorphism in organic semiconductor thin films through nanoconfinement. *J. Am. Chem. Soc.* **136**, 17046–17057 (2014).
- Wang, L., Ölivier, Y., Prezhdo, O. V. & Beljonne, D. Maximizing singlet fission by intermolecular packing. J. Phys. Chem. Lett. 5, 3345–3353 (2014).
- 44. Wilson, M. W. et al. Ultrafast dynamics of exciton fission in polycrystalline pentacene. *J. Am. Chem. Soc.* **133**, 11830–11833 (2011).

- 45. Tuan Trinh, M. et al. Distinct properties of the triplet pair state from singlet fission. *Sci. Adv.* **3**, e1700241 (2017).
- Pensack, R. D. et al. Observation of two triplet-pair intermediates in singlet exciton fission. J. Phys. Chem. Lett. 7, 2370–2375 (2016).
- Loukianov, A. et al. Two-dimensional electronic stark spectroscopy.
 J. Phys. Chem. Lett. 8, 679–683 (2017).
- 48. Bussolotti, F., Kera, S. & Ueno, N. Potassium doping of single crystalline pentacene thin film. *Phys. Rev. B* **86**, 155120 (2012).
- Roth, F. & Knupfer, M. Impact of potassium doping on the electronic structure of tetracene and pentacene: an electron energy-loss study. J. Chem. Phys. 143, 154708 (2015).
- McDonough, T. J. et al. Triplet exciton dissociation and electron extraction in graphene-templated pentacene observed with ultrafast spectroscopy. *Phys. Chem. Chem. Phys.* 19, 4809–4820 (2017).
- 51. Di, D. et al. Efficient triplet exciton fusion in molecularly doped polymer light-emitting diodes. *Adv. Mater.* **29**, 1–7 (2017).
- Burgos, J., Pope, M., Swenberg, C. E. & Alfano, R. R. Heterofission in pentacene-doped tetracene single crystals. *Phys. Status Solidi B* 83, 249–256 (1977).
- Stern, H. L. et al. Identification of a triplet pair intermediate in singlet exciton fission in solution. *Proc. Natl Acad. Sci. USA* 112, 7656–7661 (2015).
- 54. Kearns, N. M., Mehlenbacher, R. D., Jones, A. C. & Zanni, M. T. Broadband 2D electronic spectrometer using white light and pulse shaping: noise and signal evaluation at 1 and 100 kHz. *Opt. Express.* 25, 7869–7883 (2017).
- Sharifzadeh, S. et al. Relating the physical structure and optoelectronic function of crystalline TIPS-pentacene. *Adv. Funct. Mater.* 25, 2038–2046 (2015).
- Yamagata, H. et al. The nature of singlet excitons in oligoacene molecular crystals. J. Chem. Phys. 134, 204703 (2011).
- 57. Kistler, K. A., Pochas, C. M., Yamagata, H., Matsika, S. & Spano, F. C. Absorption, circular dichroism and photoluminescence in perylene diimide bichromophores: polarization-dependent H- and J-aggregate behavior. *J. Phys. Chem. B* 116, 77–86 (2012).
- Hestand, N. J. et al. Polarized absorption in crystalline pentacene: theory vs experiment. J. Phys. Chem. C 119, 22137–22147 (2015).
- Hestand, N. J. & Spano, F. C. Molecular aggregate photophysics beyond the Kasha model: novel design principles for organic materials. *Acc. Chem. Res.* 50, 341–350 (2017).

Acknowledgements

This research was supported by NSF CHE 1665110 and AFOSR FA9550-15-1-0061.

Author contributions

A.C.J., M.T.Z., N.M.K. and J.T.F. designed the experiment. A.C.J., N.M.K. and J.T.F. performed the measurements. A.C.J., N.M.K. and J.-J.H. performed the data analysis and modelling. A.C.J. and M.T.Z. wrote the manuscript.

Competing interests

 $\rm M.T.Z.$ is an owner of PhaseTech Spectroscopy, Inc., which sells 2D spectrometers and pulse shapers.

Additional information

Supplementary information is available for this paper at https://doi.org/10.1038/s41557-019-0368-9.

 $\textbf{Correspondence and requests for materials} \ \text{should be addressed to M.T.Z.}$

Reprints and permissions information is available at www.nature.com/reprints.

Publisher's note Springer Nature remains neutral with regard to jurisdictional claims in published maps and institutional affiliations.

© The Author(s), under exclusive licence to Springer Nature Limited 2019